condensed matter

MDPI

Article

The Multi-Detectors System of the PANDORA Facility: Focus on the Full-Field Pin-Hole CCD System for X-ray Imaging and Spectroscopy

David Mascali [1,*], Eugenia Naselli [1], Sandor Biri [2], Giorgio Finocchiaro [1,3], Alessio Galatà [4], Giorgio Sebastiano Mauro [1], Maria Mazzaglia [1], Bharat Mishra [1,3], Santi Passarello [1], Angelo Pidatella [1], Richard Rácz [2], Domenico Santonocito [1] and Giuseppe Torrisi [1]

[1] Laboratori Nazionali del Sud, Istituto Nazionale di Fisica Nucleare, Via S. Sofia 62, 95123 Catania, Italy; eugenia.naselli@lns.infn.it (E.N.); giorgio.finocchiaro@lns.infn.it (G.F.); mauro@lns.infn.it (G.S.M.); mazzaglia@lns.infn.it (M.M.); mishra@lns.infn.it (B.M.); passarello@lns.infn.it (S.P.); pidatella@lns.infn.it (A.P.); santonocito@lns.infn.it (D.S.); giuseppe.torrisi@lns.infn.it (G.T.)
[2] Institute for Nuclear Research (Atomki), Bem Square 18/c, 4026 Debrecen, Hungary; biri@atomki.hu (S.B.); rracz@atomki.mta.hu (R.R.)
[3] Dipartimento di Fisica e Astronomia, Università degli Studi di Catania, Via S. Sofia 64, 95123 Catania, Italy
[4] Laboratori Nazionali di Legnaro, Istituto Nazionale di Fisica Nucleare, Viale dell'Università, 2, 35020 Legnaro, Italy; alessio.galata@lnl.infn.it
* Correspondence: davidmascali@lns.infn.it

Abstract: PANDORA (Plasmas for Astrophysics Nuclear Decays Observation and Radiation for Archaeometry) is an INFN project aiming at measuring, for the first time, possible variations in in-plasma β-decay lifetimes in isotopes of astrophysical interest as a function of thermodynamical conditions of the in-laboratory controlled plasma environment. Theoretical predictions indicate that the ionization state can dramatically modify the β-decay lifetime (even of several orders of magnitude). The PANDORA experimental approach consists of confining a plasma able to mimic specific stellar-like conditions and measuring the nuclear decay lifetime as a function of plasma parameters. The β-decay events will be measured by detecting the γ-ray emitted by the daughter nuclei, using an array of 12 HPGe detectors placed around the magnetic trap. In this frame, plasma parameters have to be continuously monitored online. For this purpose, an innovative, non-invasive multi-diagnostic system, including high-resolution time- and space-resolved X-ray analysis, was developed, which will work synergically with the γ-rays detection system. In this contribution, we will describe this multi-diagnostics system with a focus on spatially resolved high-resolution X-ray spectroscopy. The latter is performed by a pin-hole X-ray camera setup operating in the 0.5–20 keV energy domain. The achieved spatial and energy resolutions are 450 µm and 230 eV at 8.1 keV, respectively. An analysis algorithm was specifically developed to obtain SPhC (Single Photon-Counted) images and local plasma emission spectrum in High-Dynamic-Range (HDR) mode. Thus, investigations of image regions where the emissivity can change by even orders of magnitude are now possible. Post-processing analysis is also able to remove readout noise, which is often observable and dominant at very low exposure times (ms). Several measurements have already been used in compact magnetic plasma traps, e.g., the ATOMKI ECRIS in Debrecen and the Flexible Plasma Trap at LNS. The main outcomes will be shortly presented. The collected data allowed for a quantitative and absolute evaluation of local emissivity, the elemental analysis, and the local evaluation of plasma density and temperature. This paper also discusses the new plasma emission models, implemented on PIC-ParticleInCell codes, which were developed to obtain powerful 3D maps of the X-rays emitted by the magnetically confined plasma. These data also support the evaluation procedure of spatially resolved plasma parameters from the experimental spectra as well as, in the near future, the development of appropriate algorithms for the tomographic reconstruction of plasma parameters in the X-ray domain. The described setups also include the most recent upgrade, consisting of the use of fast X-ray shutters with special triggering systems that will be routinely implemented to perform both space- and time-resolved spectroscopy during transient, stable, and turbulent plasma regimes (in the ms timescale).

Citation: Mascali, D.; Naselli, E.; Biri, S.; Finocchiaro, G.; Galatà, A.; Mauro, G.S.; Mazzaglia, M.; Mishra, B.; Passarello, S.; Pidatella, A.; et al. The Multi-Detectors System of the PANDORA Facility: Focus on the Full-Field Pin-Hole CCD System for X-ray Imaging and Spectroscopy. *Condens. Matter* **2024**, *9*, 28. https://doi.org/10.3390/condmat9020028

Academic Editor: Bernardo Barbiellini

Received: 6 April 2024
Revised: 6 June 2024
Accepted: 7 June 2024
Published: 20 June 2024

Keywords: in-plasma β-decay studies; plasma diagnostics; electron cyclotron resonance ion sources; X-ray imaging; single-photon-counted images; high dynamical range analysis; X-ray spatially resolved spectroscopy

1. Introduction

PANDORA is a facility whose construction is financed by INFN in the frame of the PANDORA_Gr3 project [1,2]. It aims to build an innovative compact and flexible magnetic plasma trap for fundamental physics studies and also interdisciplinary and applied research. A radically new and challenging approach is at the basis of the project, which aims at studying β-decays in laboratory plasma (never conducted so far), i.e., under ionization conditions that can mimic some stellar environments, relevant for the nucleosynthesis of chemical elements in the cosmos. The basic idea is that a compact plasma trap can be used to study the properties of radionuclides undergoing $\beta^{\pm}$ decay or electron capture in an environment where plasma parameters—electron density n_e, electron temperature T_e, and ion charge state distribution (CSD)—are fully under control. In such an environment, both ionizations and atomic excitations can occur, playing a relevant role in the nuclear process dynamics. Indeed, the existence of clouds of charges, both positive and negative, can induce perturbations to the atomic-level and impact-level populations, which can affect the β-decay half-life for a fixed type of transition. Takahashi and Yokoi pioneeringly investigated, in their seminal work [3], the in-plasma effects due to the temperature and the electron densities typical of stellar interiors on β-decay rates and predicted even dramatic deviations from the terrestrial values depending on the physics cases investigated. Only a few pieces of experimental evidence were collected up to now using storage rings as setups [4–6].

As for demonstrating the feasibility of the radically new experimental approach of PANDORA, a short list of case studies has been identified, including ^{94}Nb, ^{134}Cs, and ^{176}Lu. For all those three, terrestrial β-decay lifetimes and relative branchings in stellar s-processes have been investigated for a long time. Recent calculations suggest that, at electron temperatures $kT_e \sim 10$ keV corresponding to the PANDORA working conditions, their lifetimes may collapse by several orders of magnitude, making the variation measurable with this new setup [2]. In the laboratory, the plasma temperature and density can be modulated according to the RF power sustaining the plasma, the magnetic field strength, the background pressure, etc. This will allow one to characterize nuclear rates versus the plasma density and temperature in a stellar-like condition at least as it concerns the CSD (e.g., like in the stellar cores or resembling primordial nucleosynthesis conditions).

β-decay rates will be evaluated through the detection of the γ-rays emitted by the excited states of daughter nuclei in the plasma. An array of high-efficiency HPGe (High-purity Germanium) detectors placed around the magnetic trap will be used to detect these γ-rays [7]. In addition, an innovative multi-diagnostic system, which consists of dozens of non-invasive tools, was developed [8,9] and will be used to thermodynamically monitor and characterize plasma environment properties. An overview of the three main sub-systems of the PANDORA facility is shown in Figure 1.

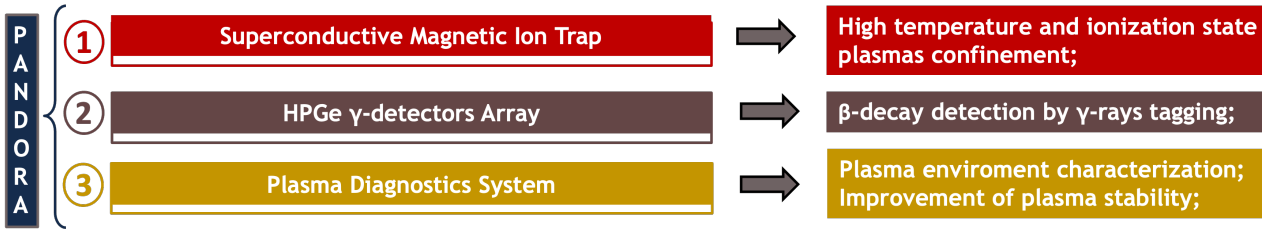

Figure 1. Summary of the three main sub-systems of the PANDORA facility.

Furthermore, studying the stellar opacity of an astrophysical scenario involved in quiescent or explosive stellar evolution becomes of fundamental importance, both for astrophysics and nuclear astrophysics interests. One example is provided by the expelled plasma matter (ejecta) from binary compact object collapse, e.g., neutron stars, the precursor of both gravitational wave events and the electromagnetic transient known as kilonovae. These latter, given a detailed reconstruction of the ejecta opacity, allow us to study the nuclei composition of the cosmic site, believed to be among the major sites of r-process nucleosynthesis. The basic idea is to exploit the plasma of PANDORA to reproduce a certain time stage of the ejecta expelled from the merging, as a function of density and temperature [10], and to measure the plasma opacity of species theoretically dominant at that time in the opacity contribution, trying to reproduce abundances of r-process elements and to improve opacity information for reproducing the kilonova light curve.

The procurement and installation at the INFN-LNS of the whole system of the PANDORA facility is expected by the middle of 2025. The first experimental measurements will be possible by the end of 2025.

2. PANDORA Experimental Setup

The PANDORA trap consists of a cylindrical discharge vessel made of stainless steel with an outer radius of 15 cm, an inner radius of 14 cm, and a length of 70 cm. The external magnetic field used for ECR (Electron Cyclotron Resonance) heating and plasma confinement is fully superconductive and consists of three solenoids for axial confinement and a hexapole for radial confinement (with a maximum field of 3.0 T along the chamber axis and 1.6 T along the chamber inner surface) [11]. Microwaves are generated by three klystrons, two operating in the frequency range from 17.3 to 18.1 at 2.4 kW of power and one operating in the frequency range of 21–22 GHz at 1.5 kW power. The superconducting magnetic plasma trap is able to produce and confine the plasmas with an electron–ion density of up to 10^{13} cm^{-3} and electron temperature of $T_e \sim 0.1$–30 keV.

Since ECR plasmas emit radiation from microwaves to hard X-rays, this radiation can be used to investigate plasma parameters in different energetic regimes. The developed advanced multi-diagnostic system includes dozens of non-invasive devices that will operate simultaneously for the non-intrusive monitoring of the thermodynamic plasma properties and the measurements of the electron plasma density and temperature. A sketch of the PANDORA facility including the superconducting magnetic system (red), the experimental setup for measuring the in-plasma activity (γ detector array), and on-line monitoring of the thermodynamic plasma parameters (i.e., two X-ray CCD cameras, an optical spectrometer, interferopolarimetry, a two-pin RF probe, and two SDDs (Silicon Drift Detectors)) is shown in Figure 2. The most relevant characteristics—in terms of sensitive range and resolution—and the experimental measurements that can be used with the typical uncertainties are summarized in Table 1 and Figure 3 (on the left for the RF, microwave, and Thomson scattering techniques and on the right for the optical, soft, and hard X-ray tools).

In more detail, the complex multi-diagnostic setup (see Figure 3 for the sketch and Table 1 for the features) will consist of the following:

1. Two spectrometers with different spectral resolutions for the plasma-emitted visible light characterization: the first is the spectrograph SARG (Spettrografo Alta Risoluzione Galileo) with a really high spectral resolution of $R = (\frac{\lambda}{\Delta\lambda}) = 160{,}000$ in the spectral range 370–900 nm [12]. Such a value allows one to identify spectral lines separated up to 0.003 nm at λ = 500 nm. By this resolution, SARG is in principle able to identify spectral line shifts (due, for example, to isotopic line shift or Doppler effects) in the order of 0.004 nm, where typical $\Delta\lambda$isot < 0.01 nm and velocity fields are down to 3 km/s, corresponding to typical ion temperatures in the order of a few eV. Also, this resolution provides reliable results in line with broadening estimates due to collisional (thermal) or Stark effects, down to 0.005 nm, or direct magnetic field estimates due to Zeeman splitting in the order of B_{min} = 0.2 T [13]. The second consists of a Horiba iHR550 spectrometer, coupled to a Synapse Horiba CCD camera, with a

nominal resolution around 0.035 nm (R = 13,900 at λ = 486 nm) in the spectral range 300–750 nm [10]. This spectrometer was already commissioned and can be considered as a complementary tool to the SARG spectrograph.

2. One Incoherent Thomson Scattering (ITS) system used for the direct and non-invasive measurement of electron properties [14]. It is made of (i) a 532 nm Quantel with a 10 Hz Nd:YAG laser of 430 mJ nominal pulse energy, (ii) an Acton Standard Series SP-2756 imaging spectrometer, equipped with three gratings in order to access different spectral ranges (and hence different ranges of electron energies), (iii) a PI-MAX 4: 1024f iCCD camera for photon detection, and (iv) a fiber bundle for light collection from the plasma volume and transmission to the camera detector (Princeton Instruments, Acton, MA, USA). The detection of scattered light occurs at an angle of 90° to the incident laser beam. The area under the spectrum can, with proper calibration, be directly related to the absolute electron density in the volume under investigation. The spectral broadening provides information on the electron energies (the electron energy distribution function), whereas the spectral shift away from the laser wavelength provides information on the global electron velocity. Using the current gratings with dispersions of 2400 lines/mm, 600 lines/mm, and 300 lines/mm, the accessible electron energies (Gaussian spectral widths σ) range from 3 to 380 eV. Another grating with the dispersion of 150 lines/mm will allow one to extend the measurement of electron energies in the range of 1500 eV.
3. Two Silicon Drift Detectors (SDDs) used to characterize the warm (0.5–30 keV) electrons in the plasma, measuring electron density and temperature [15] by comparing the experimental spectra with the theoretical ones [16]. SDDs have an energy resolution of 160 eV at 5.9 keV, a maximum quantum efficiency in the 2–30 keV energetic range (with a Be window with a thickness of 1 mm), and can operate at a high counting rate. An SDD can also operate in high vacuum conditions as it has a polymeric window which allows for investigations in the lower energy domain (starting from 0.4 keV).
4. Twelve High-purity Germanium (HPGe) detectors [7,17] with an average resolution (Full Width at Half Maximum, FWHM) lower than 2.5 keV at 1.3 MeV, placed radially around the PANDORA plasma chamber. The HPGe detectors have a length of 240 mm and a radius of 43.4 mm and are composed of a coaxial hyper-pure crystal with an ∼82 mm length and ∼38 mm radius. The cap aluminum has a thickness of 1 mm. The array of HPGe detectors will be used for the γ tagging of daughter nuclei. Moreover, the HPGe detector allows one to characterize the hot electrons population (30–400 keV) in the plasma [15,16].
5. Two X-ray pin-hole CCD systems for 2D/3D space-resolved spectroscopy. The X-ray CCD camera (SOPHIA-XO by Princeton Instruments) is made by a sensor of 27.6 × 27.6 mm and 2048 × 2048 pixels, with an optimal quantum efficiency in the range of 100 eV–30 keV and coupled with a lead pin-hole focusing system and an external X-Ray shutter. A detailed description of the X-ray pin-hole camera system will be presented in Section 3. The X-ray pin-hole camera technique allows one to characterize the plasma morphology and to perform space-resolved spectroscopy (thus evidencing the local displacement of electrons at different energies, as well as of plasma ions highlighted by fluorescence lines emission) [18,19] versus the main tuning parameters such as the pumping wave frequency and the strength of the confining magnetic field. It is very useful to investigate the dynamics of plasma versus plasma losses, and, consequently, to study how the operative parameters (the RF pumping frequency and power, magnetic field, and also phenomena such as plasma turbulence) affect the plasma confinement, stability, and turbulence onset.
6. A two-pins RF probe [20] connected to a Spectrum Analyzer (SA) in order to characterize the EM emission inside the plasma chamber performing frequency-resolved spectra. The two-pins RF probe is flexible with an outer diameter of 4 mm, a pin length of 3.5 mm, and a pin distance of 2 mm. The Spectrum Analyzer operates in the range

of 13–15 GHz with a resolution bandwidth of 3 MHz and a sweep time of 400 ms. This setup is able to detect both the main pumping RF frequency and self-plasma emitted radiations inside the plasma chamber, consisting of sub-harmonics. Since the RF plasma self-emission sub-harmonics can provide signatures of plasma kinetic instabilities (characterized by fast RF and X-ray bursts [21,22]), this tool can be used to detect and characterize turbulent plasma regimes in order to: (a) find a way to damp them [23–25] and, consequently, improve the ECRIS (ECR ion source) stability performances [26,27], and (b) reproduce and study these interesting phenomena of interest for astrophysics (such as the so-called Cyclotron Maser Instability, which is a typical kinetic turbulence occurring in astrophysical objects [28]) in laboratory plasmas. The two-pins RF probe connected with the scope and HPGe detector allows one to investigate plasma instability regimes. The radiofrequency and X-ray bursts produced by the unstable plasma can be characterized in a time-resolved way.

7. A W-band superheterodyne polarimeter for the measurement of the total line-integrated electron density based on the measurement of the Faraday rotation. The new design involves the use of a THz polarimetry system based on the superheterodyne approach and on the measurement of the Lissajous figures [29]. The system consists of a signal generator for the probing wave and two high-directivity horn antennas, of which the rotatable receiving antenna is connected with an orthomode transducer (OMT) (a waveguide component to combine or separate two orthogonally polarized microwave signal paths). The setup operates following the superheterodyne scheme, which allows one to downshift the detected frequency (1 GHz) compared to the probing one (100 GHz) to be detected in a scope, or through a diode by a different approach [30].

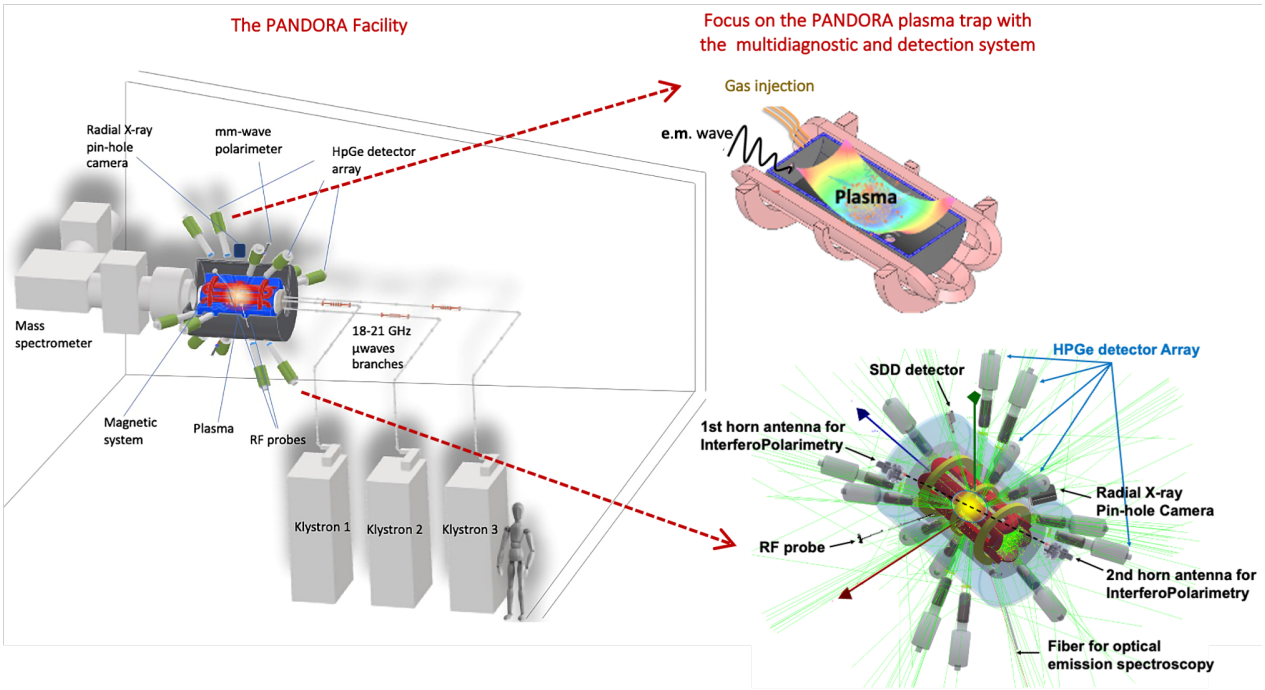

Figure 2. Rendering of the PANDORA facility including details of the superconducting magnetic system (red), the experimental setup for measuring the in-plasma activity (14 HPGe detector array), and on-line monitoring thermodynamic plasma parameters (multi-diagnostic system).

Table 1. The most relevant characteristics in terms of sensitive range, resolution, and experimental measurements that can be used with the typical uncertainties for each tool and technique.

Diagnostic Tool	Sensitive Range	Measurement	Resolution-Measure Error
2 visible light camera	1–12 eV	Optical Emission Spectroscopy: cold electrons' temperature and density	$\Delta\lambda$ = 0.035 nm R = 13,900
1 Inelastic Thomson Scattering	0.5–500 eV	EEDF, absolute electron density	Condition-dependent (a function of spectral width, dependent on temperature, and area, dependent on density
2 SDD	1–30 keV	Volumetric soft X-ray spectroscopy: warm electrons' temperature and density	Resolution∼120 eV $\epsilon_{ne} \sim 7\%, \epsilon_{Te} \sim 5\%$
12 HPGe detector	30–2000 keV	Volumetric hard X-ray spectroscopy: hot electrons' temperature and density	* FWHM < 2.4 keV $\epsilon_{ne} \sim 7\%, \epsilon_{Te} \sim 5\%$
2 X-ray pin-hole camera	2–15 keV	2D space-resolved spectroscopy and soft X-ray imaging	Energy resolution∼0.3 k Spatial resolution∼0.5 mm
2 Multi-pins RF probe	10–26.5 GHz	Local EM field intensity	$\epsilon \sim$ 0.073–0.138 dB
Multi-pins RF probe + Spectrum Analyzer (SA)	10–26.5 GHz (probe range)	Frequency-domain RF wave	SA resolution bandwidth: RBW = 3 MHz
Multi-pins RF probe + Scope + HPGe detector	10–26.5 GHz (probe range)	Time-resolved RF burst and X-ray time-resolved spectroscopy	80 Gs/s (scope) Time scales below ns
Multi-pins RF probe + X-ray pin-hole camera	10–26.5 GHz (probe range)	Time-resolved RF burst and X-ray spatial and time-resolved spectroscopy	80 Gs/s (scope) Time scales below ns
Microwave Imaging Profilometry (MIP)	60–100 GHz	Electron density profile	$\epsilon_{ne} \sim$ 1–13%
1 W-band superheterodyne polarimeter	W-band 90–100 GHz	Plasma-induced Faraday rotation: line-integrated electron density	$\epsilon_{ne} \sim$ 25%

* @ 1332.5 keV.

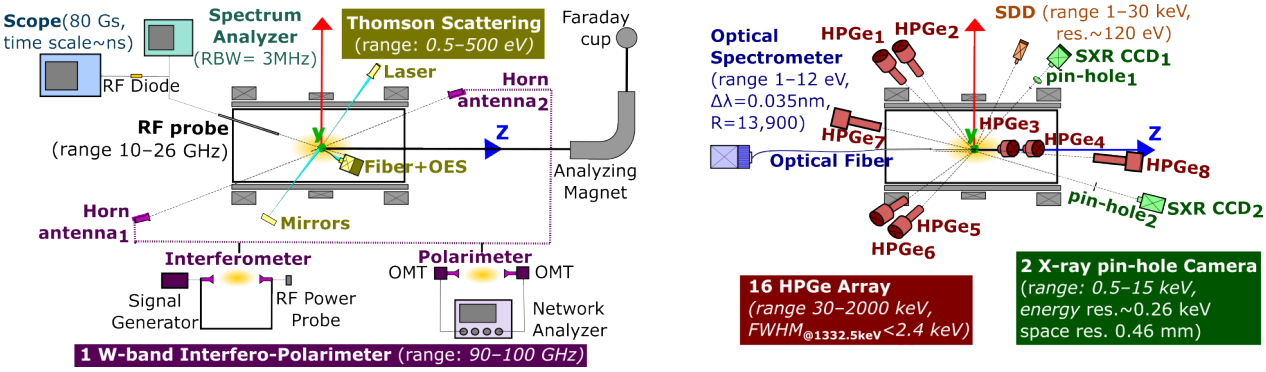

Figure 3. Sketch of the multi-diagnostic setup consisting of a collection of non-invasive tools. The RF, microwave, and Thomson scattering techniques are shown on the left and the optical, soft, and hard X-ray tools are illustrated on the right.

3. X-ray Pin-Hole Camera Measurements on the Flexible Plasma Trap Setup

The multi-diagnostic setup can be adapted to plasma traps and/or ECR ion sources of different sizes and features. Preliminary measurements were carried out on the Flexible Plasma Trap (FPT), installed at INFN-LNS. Figure 4 shows a schematic diagram of the FPT, including the multi-diagnostic setup.

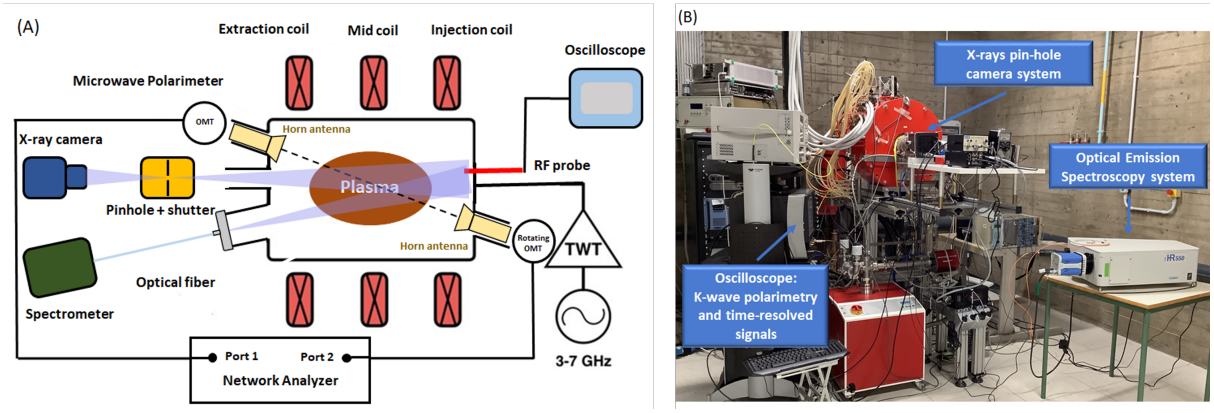

Figure 4. Sketch (**A**) and picture (**B**) of the FPT, including the multi-diagnostic setup.

The FPT consists of a cylindrical discharge vessel made of stainless steel with a radius of 41 mm and a length of 260 mm [10]. The external magnetic field used for ECR heating and plasma confinement is generated by means of three solenoids (with a maximum field of around 0.5 T), which also allow for the tuning of the magnetic profile. Microwaves are generated by a Traveling Wave Tube (TWT) operating in a range from 3 to 7 GHz. The operative values of microwave power are in the range from 0 to 400 W.

X-ray Pin-Hole Camera

Among other techniques, X-ray plasma diagnostics were developed over the years, allowing for the volumetric characterization of ECR plasmas. The volume-integrated X-ray diagnostics in the soft-X domain (from 1 keV to 30 keV) were adopted to estimate the spectral temperatures in different plasma conditions and various ECR setups vs RF power, gas pressure, and the magnetic field profile [16,31–39].

The work on X-ray imaging techniques was initiated by our team around 20 years ago ([39,40]), and the same techniques have also been used in other plasma-based facilities, enabling the morphological study of different kinds of magnetically confined plasmas, evidencing their overall structure and the spatial distribution of the warmer electrons, which play a main role in leading to X-ray emission via characteristic lines and bremsstrahlung radiation [40–48].

The X-ray full-field pin-hole CCD system is a powerful technique for space-resolved spectroscopy and spectrally resolved imaging in the soft X-ray domain (0.5–20 keV). It consists of a CCD camera (Sophia–Princeton with 4 megapixels, a 13.5 µm pixel size, and high frame rates of 8 MHz with up to four-port readout) coupled to a pin-hole focusing system and an external X-ray shutter. The focal system consists of a pin-hole (a lead disk 2 mm thick with a circular hole of 400 µm) coupled to an aluminum window, 0.8 µm thick, in order to stop low-energy photons ($E < 200$ eV). In addition, in order to reduce the multi-scattering noise and improve the signal-to-background ratio, a lead disk collimator (1 mm of thickness and 5 mm of hole diameter) was located at distances of 40 mm from the pin-hole on the CCD side. A mechanical holder was specifically designed to install in a vacuum the whole system (the Pt-Ir shutter, Pb pin-hole, Al window, and Pb collimator). A sketch is shown in Figure 5.

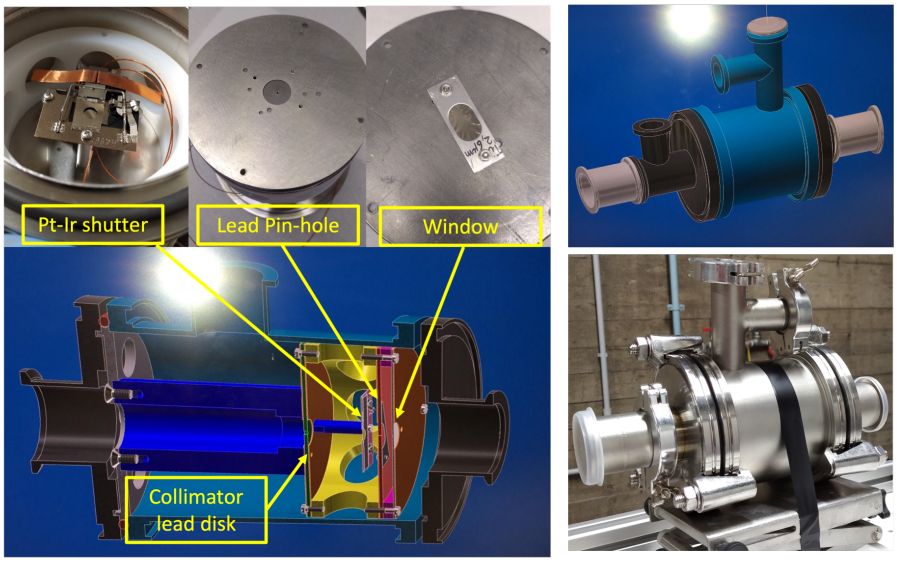

Figure 5. Pictures and mechanical drawings of the holder for the pin-hole CCD system, which houses the lead pin-hole, X-ray shutter, window, and collimator.

The X-ray shutter is made of platinum–iridium (Pt-Ir) and has an aperture diameter of 6 mm. It is capable of blocking X-ray energy up to 30 keV, and the total opening time is 4.4 ms. It was installed, tested, and used during the experiment in order to block X-rays up to 30 keV of energy during the camera readout time and optimize the performances of the pin-hole CCD camera setup, diminishing the readout noise and thus increasing the space resolution. The shutter opening is synchronized with the CCD's exposure and readout (minimum exposure time of 10 ms). The sketch of the diagnostic setup used to perform high-resolution X-ray imaging is shown in Figure 6.

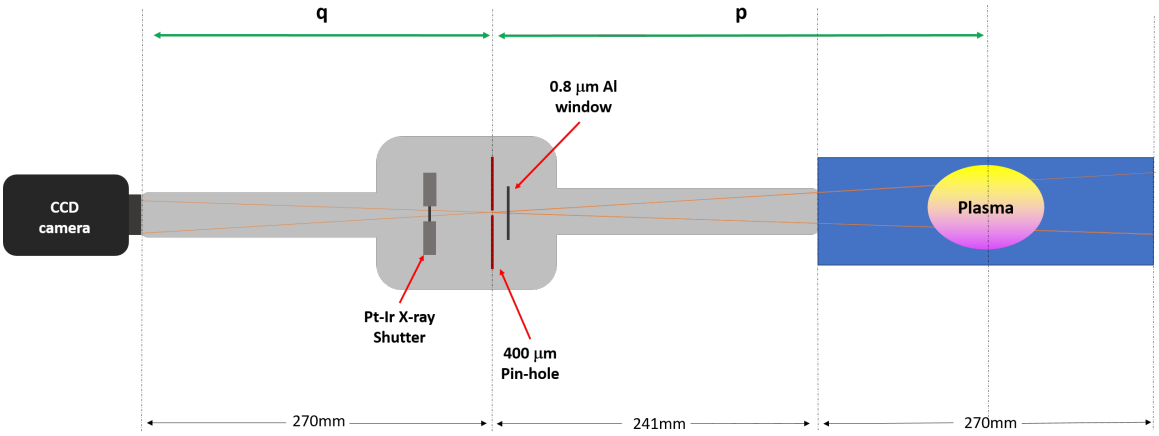

Figure 6. Sketch of the pin-hole CCD system.

The best cone of view intercepting the plasma was defined using a magnification M = 0.72 defined by the ratio q/p, where p = 376 mm and q = 270 mm are the distances center of the plasma chamber pin-hole and pin-hole CCD, respectively. Measurements were performed in Single Photon Counting (SPhC), allowing us to make energy-resolved imaging.

We developed a specific imaging algorithm [49] in order to recognize overflowed pixel clusters for each photon and discard overlapped not-photon-counted events. The choice of the exposure time is relevant to optimize the method: the SPhC condition requires a low rate of overlapped events, which would be discarded. This method makes it possible to generate space-resolved energy spectra and recognize the characteristic fluorescence

emission by plasma elements also distinguishing the radiation coming from the losses due to the deconfined electrons that impact the plasma chamber walls. The main steps are reported in the following:

- *Image Acquisition*:
  Recorded thousands of images with very short exposure times (tens to hundreds of milliseconds). Purpose: minimize the chance of multiple photons hitting the same or neighboring pixels in each image frame.
- *Grouping/Clustering Process (Gr-p)*:
  Necessary even with small exposure times due to occasional pixel clusters' overlap. Purpose: ensure direct proportionality between Analog-to-Digital Units (ADU) and single-photon energy. Objective: Assign the charge of a pixel cluster to a single photon-detection event. Overlapped clusters are discarded.
- *Algorithm Input Parameters*:
  S parameter: Maximum cluster size (in pixels) considered as a single-photon event. Larger clusters are filtered out. L parameter: it is a threshold to remove noise.
- *Scanning and Processing*:
  Code scans each image pixel-by-pixel and processes each group of neighboring pixels to determine if they represent a single- or multiple-hit event. During scanning, assigns a variable N to each coordinate (X, Y) in the CCD matrix. N represents the number of photons with energy E detected at position (X, Y). N is incremented if a photon of energy E is detected in the same position in another frame K.
- *Result*:
  After scanning all frames, a dataset made of a multi-dimensional array (X, Y, E, Ntot) is obtained. Ntot is the total number of photons with energy E at position (X, Y). Plotting Ntot vs. E over the whole image provides the full X-ray spectrum for the full-frame CCD.
- *Energy-Filtered Imaging*:
  Selects pixels in an image with energy corresponding to a specific ΔE. Selecting energy intervals corresponding to fluorescence peaks provides images of the distribution of a single element's fluorescence. For example, when applying energy filters in the Ar-Kα and Kβ lines range, the spatial distribution of Ar-plasma can be visualized. Similar filters for Ti or Ta lines visualize X-radiation from chamber walls.

The first data acquisitions were performed at the lowest exposure time allowed by the shutter (10 ms). Figure 7 (middle) shows an SPhC image obtained by processing 2000 image frames for a total exposure time of 20 s.

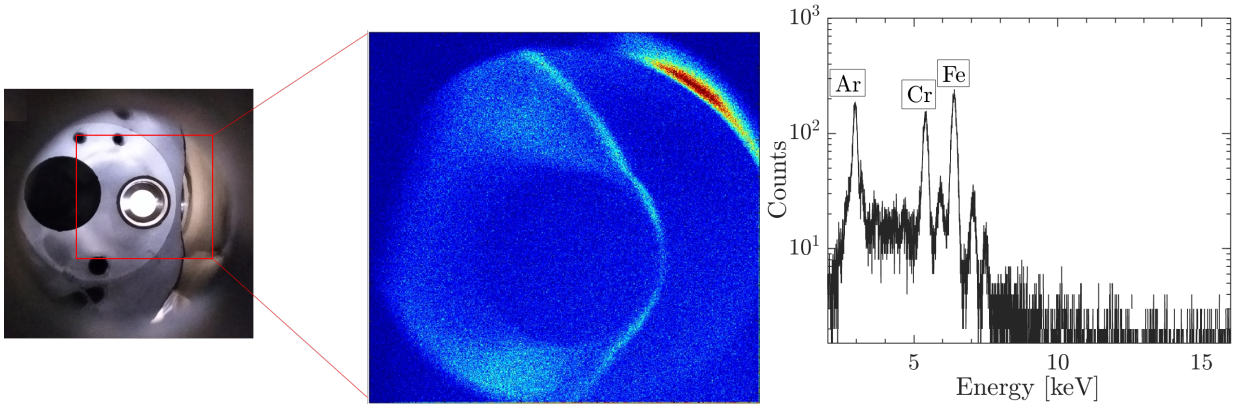

Figure 7. Field of view in the visible light (**left**) on FPT measurements, typical X-ray image (**middle**), and respective energy spectrum (**right**).

The energy spectrum integrated into the whole frame shows the fluorescence emission of the excited elements: Argon from the plasma and Chromium and Iron from the vacuum chamber (see Figure 7 (right)).

Energy calibration was performed by recognizing the K_α fluorescence emission of these elements. On one hand, regions of interest (ROIs) selection in these spectra makes energy-resolved imaging possible to investigate the spatial features of plasmas. On the other hand, if we select energy intervals corresponding to a specific fluorescence peak, it is possible to obtain the image of the selected element only. The result of ROI selection is shown in Figure 8, where Argon emission (left) is compared with the emission due to the fluorescence from Iron and Chromium (right).

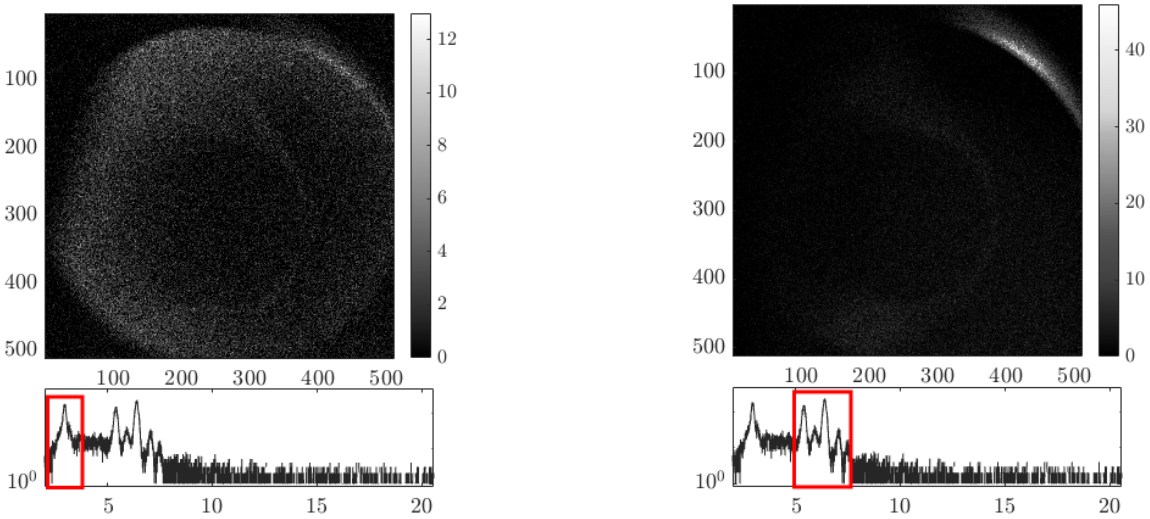

Figure 8. Energy-filtered imaging on FPT measurements: X-ray energy-filtered images in the emission of Argon plasma (**left**) and steel plasma chamber materials (**right**). Respective energy spectrum with ROI selection (bottom panels).

The use of the X-ray shutter is crucial to reduce the readout noise because of the long full-frame readout time of the camera of about 2 s. The readout process of this kind of device is based on a sequential, stepwise mechanism; it involves side-scrolling of the information stored in each pixel by the reading and digitizing system. A low-readout noise-to-signal ratio is possible only when the total readout time is much lower than the exposure time; alternatively, when these two times are comparable, it is convenient to use the shutter to be synchronized in order to totally block the incoming radiation during the readout time. For the sake of comparison, the previous measurements performed at ATOMKI laboratory, without the shutter that was unavailable at that time, were strongly affected by the readout noise, producing a clearly visible ghost image (see Figure 9 (Left)). In such a case, a complex post-processing algorithm was developed to reconstruct the real image and replace the photons detected during the CCD chip scrolling. The developed algorithm is not only able to remove the readout photons (obtaining the image shown in Figure 9 (middle)) but also to recognize and replace them in the correct pixel position. The acquisition even during the readout process is in fact genuine despite being mismatched in position. It is worth highlighting that the post-processed image (see Figure 9 (right)) quality dramatically improves compared to the original quality, also increasing the spatial resolution.

In this set of measurements, plasma was studied in different experimental conditions using another CCD camera (ANDOR iKon M by Oxford Instruments of 1024 × 1024 pixels, 13.3 µm pixel size). The exposure time was 0.5 s with a readout time of 0.4 s and the magnification was M = 0.24. Single Photon Counting conditions were guaranteed by a thicker Titanium window (9.5 µm), which stopped X-rays up to 2 keV. In this case, in order to remove the readout noise and improve the signal-to-background ratio, an innovative post-processed algorithm was specifically developed [18]. A complete characterization of plasma emission vs. losses dynamics was performed [15,18], and a spatial and energetic resolution of 450 µm and 230 eV at 8.1 keV were, respectively, reached (see Figure 9 (right)). Recently, the new system with the algorithm of analysis has also allowed one to locally

investigate the plasma parameters (in terms of their electron temperature and electron and ion densities) by comparing the experimental spectrum vs. the theoretical one. A novel numerical tool was developed to analyze spatially anisotropic electron populations in ECR plasmas [50] at INFN-LNS.

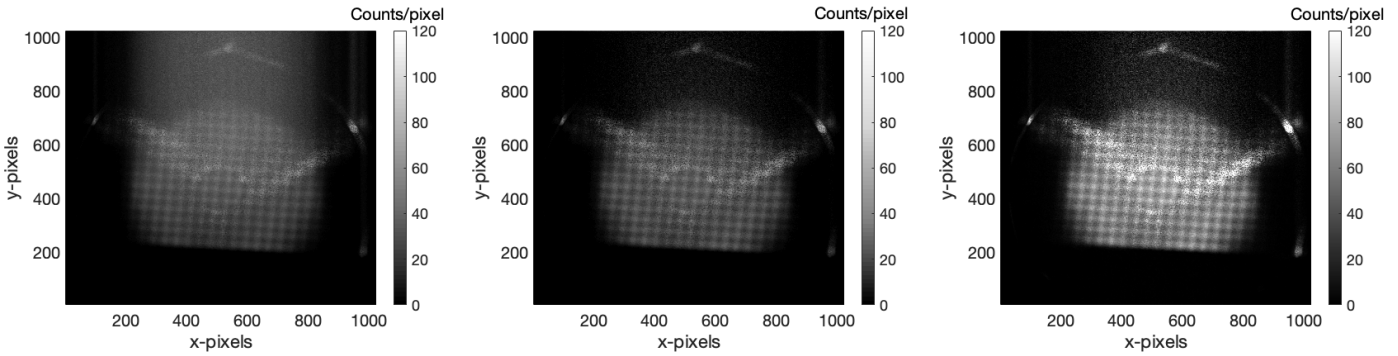

Figure 9. X-ray Argon-energy-filtered image acquired without shutter at the ATOMKI ECRIS: before (**left**) and after applying the post-processing algorithm for readout noise removal (**middle**) and readout noise replacement in the correct position (**right**).

4. X-Ray Maps for PANDORA Plasma Trap

Charged particle interactions in ECR plasmas are a rich source of radiation ranging from visible to hard X-rays, with each forming the basis for a non-intrusive diagnostic technique. When it comes to X-rays, ECR plasmas produce both line emissions and bremsstrahlung radiation—the former through collisions between ions and electrons leading to inner shell ionization and eventual fluorescence, and the latter on account of the Coulomb deceleration of electrons in the ion field. A complete qualitative and quantitative analysis of the spectra can reveal precious information about the relevant populations involved, including the ion charge state distribution (CSD), inner-shell ionization rate, particle densities, and energy distribution functions (EDFs). In the recent past, different research groups have developed plasma diagnostic tools based on X-ray emission to probe various ECRIS phenomena [37,51–53], including our group at ATOMKI, Debrecen and INFN-LNS, Catania. Our employed quasi-optical setups have been described in the previous sections [39,49,54].

Beyond indirect diagnostics, and in addition to the use of X-rays for the determination of local plasma parameters, in the PANDORA scenario, the self-emission of X-rays from the plasma forms the chief background in the high-energy spectrum where the secondary γ-photons emitted from the β-decay are located. Since the estimation of the in-plasma decay rates relies on tagging the emissivity of secondary-γ, it is imperative that the X-ray background be calculated as precisely as possible [2,7].

In order to do so, self-consistent electron simulations as those described in Ref. [55] were launched for the PANDORA design configuration, and after two exchange steps between the MATLAB© particle pusher code and COMSOL Multi-physics© FEM solver, three pairs of matrices (one each for energy and density) were obtained, corresponding to cold ($k_B T_e \sim$ 10–100 eV), warm ($k_B T_e \sim$ 100 eV–10 keV), and hot electrons ($k_B T_e \sim$ 10–100 keV). The spatial distribution of the number density n_e (in m^{-3}) and the energy density $\langle E_e \rangle$ (in eV) are shown in Figure 10. The figure serves to demonstrate the structure of ECR plasmas and the differences in the spatial distribution of the electron populations. The interaction of electrons with the resonant microwave field, superposed with their transport in the min-B magnetostatic field, leads to the formation of a central ellipsoidal region containing a bulk of the plasma electrons (called the plasmoid), and an exterior, rarified zone with extremely low density (called the halo). The boundary between the two is the resonance surface where the energy transfer between microwaves and electrons takes place. The curved trajectories in the axial and radial directions indicate the path of the electrons

along the magnetic field lines, with the star-like structure in the mid-plane representing the magnetic branches.

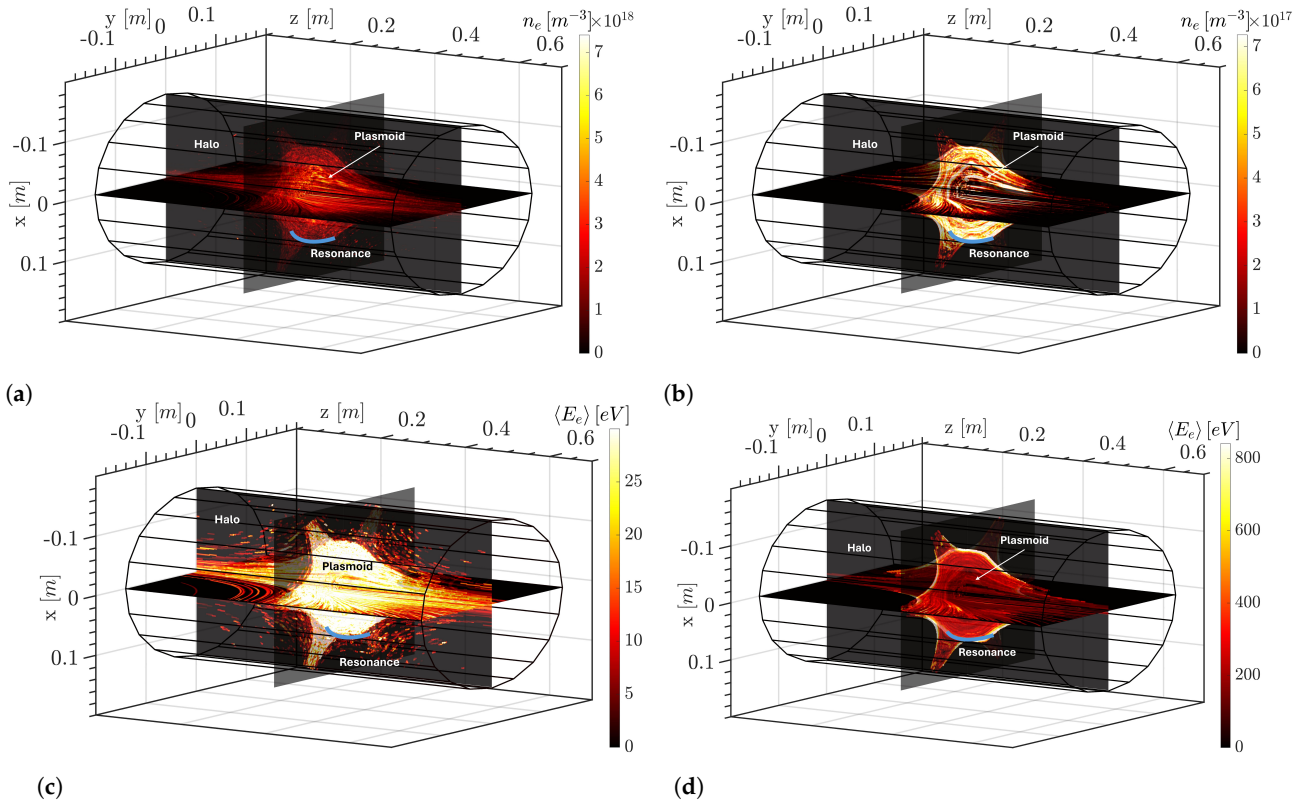

Figure 10. Number density maps of (**a**) cold electrons and (**b**) warm electrons, and energy density maps for (**c**) cold electrons and (**d**) warm electrons obtained from self-consistent PIC simulations run for the PANDORA configuration. Cold electrons are more diffuse whereas warm electrons are peaked in the off-axis region. Similarly, cold electrons show a uniform distribution of energy density, whereas that of warm electrons remains maximized near the resonance surface.

The electron number and energy density maps show that warm electrons are an order of magnitude lower in density than their cold counterparts, and their density peaks in the off-axis region (Figure 10a,b). The cold electrons are relatively more diffuse. This point can also be appreciated in Figure 10c, which shows that their energy density is spread more uniformly throughout the plasmoid whereas that of warm electrons is highly graded and peaks sharply at the resonance surface (Figure 10d), indicating an efficient coupling with the injected microwaves. These aspects can also be noted in Figure 11, which shows the radial distribution of the cold and warm electron number and energy density.

To assess the amount of radiation emitted in terms of the number of photons per unit volume per unit interval of time, the emissivity density $J(h\nu)$ was defined for the fluorescence as

$$J_{line}(h\nu) = n_e n_i \omega_{nl\to n'l'} \int_{I_{nl}}^{\infty} \sigma_{nl,ion} v_e f(E) \mathrm{d}E \quad (1)$$

where n_e, n_i are the electron and ion densities, respectively; $h\nu$ is the energy of the photon emitted during the transition $nl \rightarrow n'l'$; $\omega_{nl\to n'l'}$ is the fluorescence factor; I_{nl} is the ionization energy; $\sigma_{nl,ion}$ is the cross section for ionization from the nl atomic shell; v_e is the electron collision speed; and $f(E)$ is the electron energy distribution function (EEDF). The same for continuous bremsstrahlung emission was defined as

$$J_{brem}(h\nu) = n_e n_i h\nu \int_{h\nu}^{\infty} \frac{\mathrm{d}\sigma_K}{\mathrm{d}h\nu} v_e f(E) \mathrm{d}E \quad (2)$$

where $d\sigma_K/dh\nu$ is the differential cross section for a photon of energy $h\nu$ to be emitted after an electron collides with an ion of atomic number Z. By assuming $f(E)$ as a Maxwell distribution with $k_B T_e = (2/3)\langle E \rangle$; $Z = 8$ for O ions; and using the Lotz formula for $\sigma_{nl,ion} = \sigma_{1s,ion}$ [56], the Kramer cross section for $d\sigma_K/dh\nu$ [57], and $n_i = n_e/4$ ($\langle Z \rangle = 4$), the 3D space-resolved $J_{line}(h\nu)$ and $J_{brem}(h\nu)$ were calculated. The fluorescence lines included only the Kα from O ions (hence $nl = 1s$), whereas the bremsstrahlung was divided into two classes for a more detailed analysis—low-energy photons spanning 100 eV–3.5 keV and high-energy photons in the range 3.5–10 keV. In order to correlate electron energies with their radiation counterpart, the contribution of the three electron populations to each aforementioned radiation class was separately calculated.

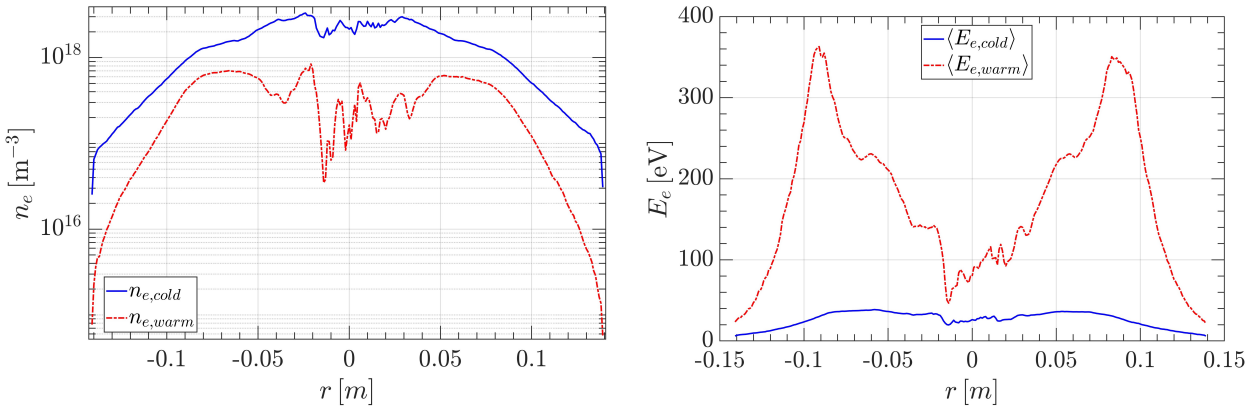

(**a**) (**b**)

Figure 11. Radial distribution of electron (**a**) number density and (**b**) energy density near the plasma mid-plane. The former is shown in log scale to highlight the difference in order of magnitude of the two populations. It can be clearly seen that cold electrons are more uniform in their properties, whereas warm electrons show signs of localization near the resonance surface ($r \sim 10$ cm).

In Figures 12 and 13, the various 3D space-resolved maps of bremsstrahlung and fluorescence as calculated using Equations (1) and (2) are shown. The contributions from both cold and warm electrons to low-energy bremsstrahlung are comparable (Figure 12a,b), whereas that of warm electrons is significantly stronger when it comes to high-energy photons (Figure 12c,d). This trend is true in the case of Kα fluorescence emissivity as well because warm electrons increase the cross section of K-shell ionization and therefore generate more fluorescence in atoms (Figure 13).

Using 3D maps of n_e and $\langle E_e \rangle$ obtained from PIC simulations and with the help of Equations (1) and (2), several virtual scenarios can be explored: (i) these data represent a valuable benchmark supporting the experimental imaging of the plasma and the local calculation of actual plasma parameters; (ii) they will be used for implementing tomographic routines assuming certain positions for the CCD cameras in the PANDORA setup; and (iii) the plasma self-emission background can be estimated at any energy and compared with expected γ-emission rates to optimize the β-decay measurement time, i.e., the signal over noise ratios. Since the electron simulations are yet ongoing and complete information on the hotter species is missing, the contribution of the same to the X-ray maps has not been taken into account but will be the subject of future work. It is expected that a significant part of the cold and warm electrons will be transferred into the hotter regime, which will not only increase plasma self-emission in the 3.5–10 keV range but also lead to significant counts well into the 2 MeV range where the secondary-γ from the decay is expected to be located [2].

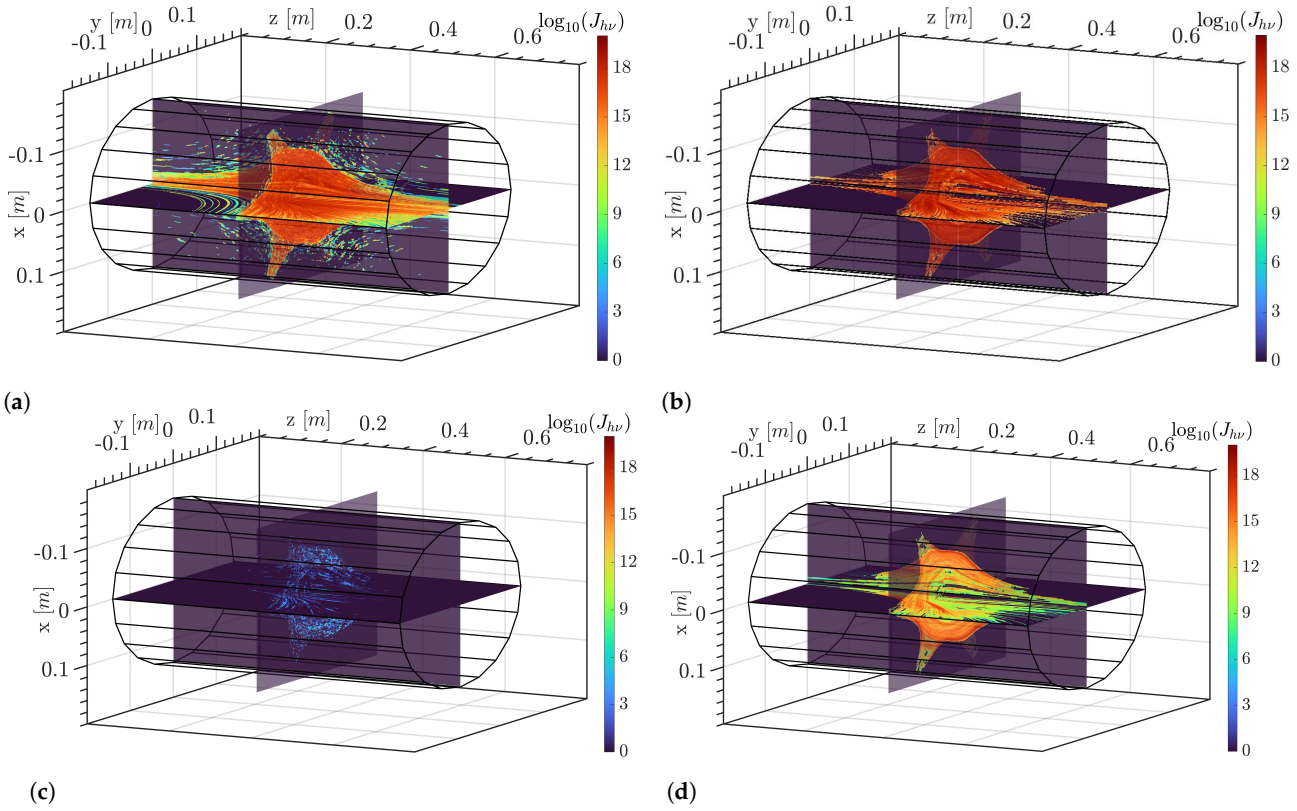

Figure 12. Maps of low-energy $J_{brem}(h\nu)$ (in $m^{-3}s^{-1}$) from (**a**) cold electrons and (**b**) warm electrons, and of high-energy $J_{brem}(h\nu)$ from (**c**) cold electrons and (**d**) warm electrons calculated using Equation (2). The colorbar is in $\log_{10}$ scale. The bremsstrahlung maps mostly mirror the spatial distribution of n_e, as long as the energy density at the point is sufficient to generate photons of the relevant energy. The emissivity peaks in the plasmoid and magnetic branches.

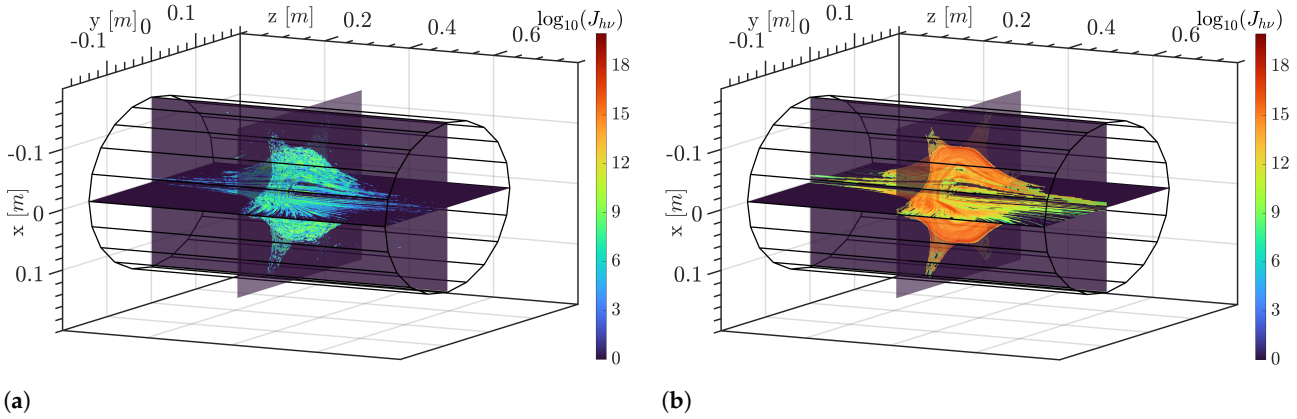

Figure 13. Maps of oxygen Kα fluorescence emissivity $J_{line}(h\nu)$ (in $m^{-3}s^{-1}$) from (**a**) cold electrons and (**b**) warm electrons calculated using Equation (1). The colorbar is in $\log_{10}$ scale. The fluorescence maps mirror the combined spatial distributions of n_e and $\langle E_e \rangle$—unlike the bremsstrahlung, the emissivity peaks in the off-axis region even for cold electrons because the near-axis region contains electrons with $\langle E_e \rangle < I_{1s}$ of oxygen.

5. Conclusions

This paper has described the multi-diagnostics setup designed and implemented in view of the PANDORA facility construction. Among the several items, including OES, interferopolarimetry, and volumetric X-ray spectroscopy, this paper has focused on the development of X-ray imaging techniques toward space- and time-resolved spectroscopy. A tool consisting of two CCD-based X-ray pin-hole cameras is now available, supported by

an advanced post-processing algorithm capable of reconstructing single-photon images in HDR mode. Energy-filtered images of the plasma were obtained and local spectra were used to evaluate thermodynamic plasma parameters, namely electron density and temperature. The up-to-date resolutions are $\delta\epsilon$ = 230 eV at 8.1 keV and $\delta\sigma$ = 450 µm and δt = 10 ms in terms of energy, spatial, and temporal resolutions, respectively. The modeling of the 3D plasma emissivity is progressing as well, and it is now possible to virtually reproduce the 3D maps of both fluorescence and bremsstrahlung emissivity of any plasma species, either in a given magnetic configuration and assuming a certain RF power for plasma ignition. This modeling is of fundamental importance to benchmark experimental data, helping in the derivation of local plasma parameters, but it will also support the tomographic reconstruction algorithms that are going to be developed in the near future. Near-term perspectives, moreover, include the implementation of AI techniques and machine learning approaches in pattern recognition in order to speed up and optimize the post-processing of single-photon-counted CCD frames.

Author Contributions: Conceptualization, D.M., E.N., S.B., G.F., A.G., B.M., R.R., A.P., D.S. and G.T.; data curation, D.M., E.N., M.M., G.F., A.G., A.P. and B.M.; formal analysis, D.M., E.N., M.M., G.F., A.P. and B.M.; funding acquisition, D.M., D.S. and S.B.; investigation, D.M, E.N., S.B., G.F., A.G., G.S.M., M.M., B.M., A.P., R.R., D.S. and G.T.; methodology, D.M., E.N., S.B., G.F., A.G., B.M., A.P. and R.R.; project administration, D.M. and D.S.; resources, D.M, E.N., S.B., G.F., A.G., G.S.M., M.M., B.M., A.P., R.R., D.S. and G.T.; software, D.M., E.N., S.B., G.F., A.G., G.S.M., M.M., B.M., S.P., A.P., R.R., D.S. and G.T.; supervision, D.M., E.N., S.B., A.P., R.R. and G.T.; visualization, D.M., E.N., S.B., G.F., A.G., G.S.M., M.M., B.M., S.P., A.P., R.R., D.S. and G.T.; writing—original draft, D.M., E.N., M.M., B.M. and G.F.; writing—review and editing, D.M., E.N., S.B., G.F., G.S.M., M.M., B.M., A.P., R.R., D.S. and G.T. All authors have read and agreed to the published version of the manuscript.

Funding: This research was funded by the European Union (NextGeneration EU) through the MUR-PNRR project SAMOTHRACE (ECS00000022) and the MUR-PNRR project PE0000023-NQSTI.

Data Availability Statement: The data that support the findings of this study are available from the corresponding author upon reasonable request.

Acknowledgments: The authors gratefully acknowledge the support of INFN by the Grants PANDORA (5th Nat. Comm.) and PANDORA_Gr3 (3rd Nat. Comm.).

Conflicts of Interest: The authors declare no conflicts of interest.

References

1. Mascali, D.; Palmerini, S.; Torrisi, G.; De Angelis, G.; Santonocito, D.; Kratz, K.-L. (Eds.) *Nuclear Physics and Astrophysics in Plasma Traps*; Frontiers Media SA: Lausanne, Switzerland, 2023
2. Mascali, D.; Santonocito, D.; Amaducci, S.; Andò, L.; Antonuccio, V.; Biri, S.; Bonanno, A.; Bonanno, V.P.; Briefi, S.; Busso, M.; et al. A Novel Approach to β-decay: PANDORA, a New Experimental Setup for Future In-Plasma Measurements. *Universe* **2022**, *8*, 80. [CrossRef]
3. Takahashi, K.; Boyd, R.N.; Mathews, G.J.; Yokoi, K. Bound-state beta decay of highly ionized atoms. *Phys. Rev. C* **1987**, *36*, 1522. [CrossRef] [PubMed]
4. Litvinov, Y.; Bosch, F.; Geissel, H.; Kurcewicz, J.; Patyk, K.; Winckler, N.; Batist, L.; Beckert, K.; Boutin, D.; Brandau, C.; et al. Measurement of the β^+ and Orbital Electron-Capture Decay Rates in Fully Ionized, Hydrogenlike, and Heliumlike ^{140}Pr Ions. *Phys. Rev. Lett.* **2007**, *99*, 262501. [CrossRef]
5. Bosch, F.; Faestermann, T.; Friese, J.; Heine, F.; Kienle, P.; Wefers, E.; Zeitelhack, K.; Beckert, K.; Franzke, B.; Klepper, O.; et al. Observation of Bound-State β^- Decay of Fully Ionized ^{187}Re:^{187}*Re*-^{187}Os Cosmochronometry. *Phys. Rev. Lett.* **1996**, *77*, 5190. [CrossRef] [PubMed]
6. Jung, M.; Bosch, F.; Beckert, K.; Eickhoff, H.; Folger, H.; Franzke, B.; Gruber, A.; Kienle, P.; Klepper, O.; Koenig, W. ; et al. First observation of bound-state β^- decay. *Phys. Rev. Lett.* **1992**, *69*, 2164. [CrossRef] [PubMed]
7. Naselli, E.; Santonocito, D.; Amaducci, S.; Celona, L.; Galatà, A.; Goasduff, A.; Mauro, G.S.; Mazzaglia, M.; Mishra, B.; Napoli, D.R.; et al. Design study of a HPGe detector array for β-decay investigation in laboratory ECR plasmas. *Front. Phys.* **2022**, *10*, 935728. [CrossRef]
8. Naselli, E.; Mascali, D.; Biri, S.; Caliri, C.; Castro, G.; Celona, L.; Cosentino, L.G.; Galatà, A.; Gammino, S.; Giarrusso, M.; et al. Multidiagnostics setups for magnetoplasmas devoted to astrophysics and nuclear astrophysics research in compact traps. *J. Instrum.* **2019**, *14*, 10008. [CrossRef]

9. Mascali, D.; Naselli, E.; Torrisi, G. Microwave techniques for electron cyclotron resonance plasma diagnostics. *Rev. Sci. Instrum.* **2022**, *93*, 033302. [CrossRef] [PubMed]
10. Pidatella, A.; Mascali, D.; Bezmalinovich, M.; Emma, G.; Mazzaglia, M.; Mishra, B.; Finocchiaro, G.; Galatà, A.; Marletta, S.; Mauro, G.S.; et al. Experimental and numerical investigation of magneto-plasma optical properties toward measurements of opacity relevant for compact binary objects. *Front. Astron. Space Sci.* **2022**, *9*, 931744. [CrossRef]
11. Mauro, G.; Celona, L.; Torrisi, G.; Pidatella, A.; Naselli, E.; Russo, F.; Mazzaglia, M.; Galatà, A.; Maimone, F.; Lang, R.; et al. An Innovative Superconducting Magnetic Trap for Probing β-decay in Plasmas. *Front. Phys.* **2022**, *10*, 931953. [CrossRef]
12. Gratton, R.G.; Bonanno, G.; Bruno, P.; CalÍ, A.; Claudi, R.U.; Cosentino, R.; Desidera, S.; Diego, F.; Farisato, G.; Martorana, G.; et al. SARG: The High Resolution Spectrograph of TNG. *Exp. Astron.* **2001**, *12*, 107–143. [CrossRef]
13. Giarrusso, M.; Avila, G.; Del Zanna, G.; Landi, E.; Leone, F.; Munari, M.; Castro, G.; Celona, L.; Gammino, S.; Mascali, D.; et al. High resolution spectropolarimetry: From Astrophysics to ECR plasmas. *J. Instrum.* **2018**, *13*, C11020. [CrossRef]
14. Tsikata, S.; Maunoury, L.; Ducret, J.-E. Incoherent Thomson scattering: Future implementation and measurement capabilities on the PANDORA experiment. *Front. Astron. Space Sci.* **2022**, *9*, 936532. [CrossRef]
15. Mascali, D.; Castro, G.; Altana, C.; Caliri, C.; Mazzaglia, M.; Romano, F.P.; Leone, F.; Musumarra, A.; Naselli, E.; Reitano, R.; et al. Electromagnetic diagnostics of ECR-Ion Sources plasmas: Optical/X-ray imaging and spectroscopy. *J. Instrum.* **2017**, *12*, C12047. [CrossRef]
16. Gumberidze, A.; Trassinelli, M.; Adrouche, N.; Szabo, C.I.; Indelicato, P.; Haranger, F.; Isac, J.-M.I.; Lamour, E.; Le Bigot, E.-O.; Mérot, J.; et al. Electronic temperatures, densities, and plasma X-ray emission of a 14.5 GHz electron-cyclotron resonance ion source. *Rev. Sci. Instrum.* **2010**, *81*, 033303. [CrossRef] [PubMed]
17. Goasduff, A.; Santonocito, D.; Menegazzo, R.; Capra, S.; Pullia, A.; Raniero, W.; Rosso, D.; Toniolo, N.; Zago, L.; Naselli, E.; et al. A high resolution γ-ray array for the pandora plasma trap. *Front. Phys.* **2022**, *10*, 936081. [CrossRef]
18. Naselli, E.; Rácz, R.; Biri, S.; Mazzaglia, M.; Galat'a, A.; Celona, L.; Gammino, S.; Torrisi, G.; Mascali, D. Quantitative analysis of an ECR Ar plasma structure by X-ray spectroscopy at high spatial resolution. *J. Instrum.* **2022**, *17*, C01009. [CrossRef]
19. Biri, S.; Rácz, R.; Perduk, Z.; Pálinkás, J.; Naselli, E.; Mazzaglia, M.; Torrisi, G.; Castro, G.; Celona, L.; Gammino, S.; et al. Innovative experimental setup for X-ray imaging to study energetic magnetized plasmas. *J. Instrum.* **2021**, *16*, P03003. [CrossRef]
20. Torrisi, G.; Mascali, D.; Sorbello, G.; Castro, G.; Celona, L.; Gammino, S. Numerical and Experimental Characterization of RF Waves Propagation in Ion Sources Magnetoplasmas. *IEEE Trans. Antennas Propag.* **2019**, *67*, 2884807. [CrossRef]
21. Shalashov, A.G.; Viktorov, M.E.; Mansfeld, D.A.; Golubev, S.V. Kinetic instabilities in a mirror-confined plasma sustained by high-power microwave radiation. *Phys. Plasmas* **2017**, *24*, 032111. [CrossRef]
22. Izotov, I.; Tarvainen, O.; Mansfeld, D.; Skalyga, V.; Koivisto, H.; Kalvas, T.; Komppula, J.; Kronholm, R.; Laulainen, J. Microwave emission related to cyclotron instabilities in a minimum-B electron cyclotron resonance ion source plasma. *Plasma Sources Sci. Technol.* **2015**, *24*, 045017. [CrossRef]
23. Naselli, E.; Mascali, D.; Mazzaglia, M.; Biri, S.; Rácz, R.; Pálinkás, J.; Perduk, Z.; Galatá, A.; Castro, G.; Celona, L.; et al. Impact of two-close-frequency heating on ECR ion source plasma radio emission and stability. *Plasma Sources Sci. Technol.* **2019**, *28*, 085021. [CrossRef]
24. Rácz, R.; Biri, S.; Perduk, Z.; Pálinkás, J.; Mascali, D.; Mazzaglia, M.; Naselli, E.; Torrisi, G.; Castro, G.; Celona, L.; et al. Effect of the two-close-frequency heating to the extracted ion beam and to the X-ray flux emitted by the ECR plasma. *J. Instrum.* **2018**, *13*, C12012. [CrossRef]
25. Mascali, D.; Naselli, E.; Rácz, R.; Biri, S.; Celona, L.; Galatà, A.; Gammino, S.; Mazzaglia, M.; Torrisi, G. Experimental study of single vs. two-close-frequency heating impact on confinement and losses dynamics in ECR Ion Sources plasmas by means of X-ray spectroscopy and imaging. *Plasma Phys. Control. Fusion* **2022**, *64*, 035020. [CrossRef]
26. Gammino, S.; Mascali, D.; Celona, L.; Maimone, F.; Ciavola, G. Considerations on the role of the magnetic field gradient in ECR ion sources and build-up of hot electron component. *Plasma Sources Sci. Technol.* **2009**, *18*, 045016. [CrossRef]
27. Tarvainen, O.; Izotov, I.; Mansfeld, D.; Skalyga, V.; Golubev, S.; Kalvas, T.; Koivisto, H.; Komppula, J.; Kronholm, R.; Laulainen, J.; et al. Beam current oscillations driven by cyclotron instabilities in a minimum-B electron cyclotron resonance ion source plasma. *Plasma Sources Sci. Technol.* **2014**, *23*, 025020. [CrossRef]
28. Zhao, G.Q.; Feng, H.Q.; Wu, D.J.; Chen, L.; Tang, J.F.; Liu, Q. Cyclotron maser emission from power-law electrons with strong pitch-angle anisotropy. *Astrophys. J.* **2016**, *822*, 58. [CrossRef]
29. Torrisi, G.; Naselli, E.; Mascali, D.; Di Donato, L.; Sorbello, G. Mm-wave polarimeter and profilometry design study for retrieving plasma density in the PANDORA experiment. *Front. Astron. Space Sci.* **2022**, *9*, 949920. [CrossRef]
30. Cano, J.L.; Villa, E.; Teran, V.; Gonzalez, E.; De la Fuente, L.; Artal, E.; Mediavilla, A. A W-band polarimeter for radio astronomy applications: Design and simulation. In Proceedings of the International Conference on Electromagnetics in Advanced Applications (ICEAA), Torino, Italy, 7–11 September 2015; pp. 452–455.
31. Fantz, U.; Tarvainen, O. Preface for the special topic on "ion source diagnostics". *Rev. Sci. Instrum.* **2022**, *93*, 101601. [CrossRef] [PubMed]
32. Thuillier, T.; Benitez, J.; Biri, S.; Rácz, R. X-ray diagnostics of ECR ion sources—Techniques, results, and challenges. *Rev. Sci. Instrum.* **2022**, *93*, 021102. [CrossRef]
33. Nebem, D.; Fogleman, J.; Isherwood, B.; Leitner, D.; Machicoane, G.; Renteria, S.; Stetson, J.; Tobos, L. X-ray investigation on the Superconducting Source for Ions (SuSI). *JINST* **2019**, *14*, C02008. [CrossRef]

34. Li, J.B.; Li, L.X.; Li, L.B.; Guo, J.W.; Hitz, D.; Lu, W.; Feng, J.C.; Zhang, W.H.; Zhang, X.Z.; Zhao, H.Y.; et al. Influence of electron cyclotron resonance ion source parameters on high energy electrons. *Rev. Sci. Instrum.* **2020**, *91*, 083302. [CrossRef] [PubMed]
35. Barué, C.; Lamoureux, M.; Briand, P.; Girard, A.; Melin, G. Investigation of hot electrons in electron-cyclotron-resonance ion sources. *J. Appl. Phys.* **1994**, *76*, 2662. [CrossRef]
36. Ropponen, T.; Tarvainen, O.; Izotov, I.; Noland, J.; Toivanen, V.; Machicoane, G.; Leitner, D.; Koivisto, H.; Kalvas, T.; Peura, P.; et al. Studies of plasma breakdown and electron heating on a 14 GHz ECR ion source through measurement of plasma bremsstrahlung. *Plasma Sources Sci. Technol.* **2011**, *20*, 055007. [CrossRef]
37. Isherwood, B.; Machicoane, G. Measurement of the energy distribution of electrons escaping confinement from an electron cyclotron resonance ion source. *Rev. Sci. Instrum.* **2020**, *91*, 025104. [CrossRef]
38. Benitez, J.; Lyneis, C.; Phair, L.; Todd, D.; Xie, D. Dependence of the bremsstrahlung spectral temperature in minimum-B electron cyclotron resonance ion sources. *IEEE Trans. Plasma Sci.* **2017**, *45*, 1746. [CrossRef]
39. Rácz, R.; Biri, S.; Pxaxlinkxaxs, J.; Mascali, D.; Castro, G.; Caliri, C.; Romano, F.P.; Gammino, S. X-ray pinhole camera setups used in the Atomki ECR Laboratory for plasma diagnostics. *Rev. Sci. Instrum.* **2016**, *87*, 02A741. [CrossRef] [PubMed]
40. Biri, S.; Valek, A.; Suta, T.; Takács, E.; Szabó, C.; Hudson, L.T.; Radics, B.; Imrek, J.; Juhász, B.; Pálinkás, J. Imaging of ECR plasmas with a pinhole X-ray camera. *Rev. Sci. Instrum.* **2004**, *75*, 1420. [CrossRef]
41. Anton, M.; Weisen, H.; Dutch, M.J.; Von Der Linden, W.; Buhlmann, F.; Chavan, R.; Marletaz, B.; Marmillod, P.; Paris, P. X-ray tomography on the TCV tokamak. *Plasma Phys. Control. Fusion* **1996**, *1849*, 38. [CrossRef]
42. Petrasso, R.; Gerassimenko, M.; Seguin, F.H.; Ting, J.; Krogstad, R.; Gauthier, P.; Hamilton, W.; Ramsey, A.T.; Burstein, P.; Granetz, R. Soft x-ray imaging instrument for the Alcator A tokamak. *Rev. Sci. Instrum.* **1980**, *51*, 585–590. [CrossRef]
43. Pacella, D.; Leigheb, M.; Bellazzini, R.; Brez, A.; Finkenthal, M.; Stutman, D.; Kaita, R.; Sabbagh, S.A. Soft X-ray tangential imaging of the NSTX core plasma by means of an MPGD pinhole camera. *Plasma Phys. Control. Fusion* **2004**, *46*, 1075. [CrossRef]
44. Jang, S.; Lee, S.G.; Lim, C.H.; Kim, H.O.; Kim, S.Y.; Lee, S.H.; Hong, J.; Jang, J.; Jeon, T.; Moon, M.K.M.; et al. Preliminary result of an advanced tangential X-ray pinhole camera system with a duplex MWPC on KSTAR plasma. *Curr. Appl. Phys.* **2013**, *13*, 5. [CrossRef]
45. Song, I.; Jang, J.; Jeon, T.; Pacella, D.; Claps, G.; Murtas, F.; Lee, S.H.; Choe, W. Tomographic 2-D X-ray imaging of toroidal fusion plasma using a tangential pinhole camera with gas electron multiplier detector. *Curr. Appl. Phys.* **2016**, *16*, 10. [CrossRef]
46. Pablant, N.A.; Delgado-Aparicio, L.; Bitter, M.; Brandstetter, S.; Eikenberry, E.; Ellis, R.; Hill, K.W.; Hofer, P.; Schneebeli, M. Novel energy resolving X-ray pinhole camera on Alcator C-Mod. *Rev. Sci. Instrum.* **2012**, *83*, 10E526. [CrossRef] [PubMed]
47. Takács, E.; Radics, B.; Szabó, C.I.; Biri, S.; Hudson, L.T.; Imrek, J.; Juhász, B.; Suta, T.; Valek, A.; Pálinkás, J. Spatially resolved x-ray spectroscopy of an ECR plasma–indication for evaporative cooling. *Nucl. Instrum. Methods Phys. Res.* **2005**, *235*, 120–125. [CrossRef]
48. McPherson, L.A.; Ampleford, D.J.; Coverdale, C.A.; Argo, J.W.; Owen, A.C.; Jaramillo, D.M. High energy X-ray pinhole imaging at the Z facility. *Rev. Sci. Instrum.* **2016**, *87*, 063502. [CrossRef] [PubMed]
49. Naselli, E.; Ràcz, R.; Biri, S.; Mazzaglia, M.; Celona, L.; Gammino, S.; Torrisi, G.; Perduk, Z.; Galatxax, A.; Mascali, D. Innovative analytical method for X-ray imaging and space-resolved spectroscopy of ECR plasmas. *Condens. Matter* **2022**, *7*, 5. [CrossRef]
50. Mishra, B.; Pidatella, A.; Biri, S.; Galatà, A.; Naselli, E.; Rácz, R.; Torrisi, G.; Mascali, D. A novel numerical tool to study electron energy distribution functions of spatially anisotropic and non-homogeneous ECR plasmas. *Phys. Plasmas* **2021**, *28*, 102509. [CrossRef]
51. Douysset, G.; Khodja, H.; Girard, A.; Briand, J.P. Highly charged ion densities and ion confinement properties in an electron-cyclotron-resonance ion source. *Phys. Rev. E* **2000**, *61*, 3. [CrossRef]
52. Santos, J.P.; Costa, A.M.; Marques, J.P.; Martins, M.C.; Indelicato, P.; Parente, F. X-ray-spectroscopy analysis of electron-cyclotron-resonance ion-source plasmas. *Phys. Rev. A* **2010**, *82*, 062516. [CrossRef]
53. Sakildien, M.; Kronholm, R.; Tarvainen, O.; Kalvas, T.; Jones, P.; Thomae, R.; Koivisto, H. Inner shell ionization of argon in ECRIS plasma. *Nucl. Inst. Methods Phys. Res. A* **2018**, *900*, 40–52. [CrossRef]
54. Mishra, B.; Pidatella, A.; Galatà, A.; Biri, S.; Rácz, R.; Naselli, E.; Mazzaglia, M.; Torrisi, G.; Mascali, D. Probing Electron Properties in ECR Plasmas Using X-ray Bremsstrahlung and Fluorescence Emission. *Condens. Matter* **2021**, *6*, 41. [CrossRef]
55. Galatà, A.; Mascali, D.; Mishra, B.; Naselli, E.; Pidatella, A.; Torrisi, G. On the Numerical Determination of the Density and Energy Spatial Distributions relevant for in-Plasma β-Decay Emission Estimation. *Front. Phys.* **2022**, *10*, 947194.
56. Lotz, W. Electron-impact ionization cross-sections for atoms up to Z=108. *Z. Phys.* **1970**, *232*, 101–107. [CrossRef]
57. Kramers, H. XCIII. On the theory of X-ray absorption and of the continuous X-ray spectrum. *Lond. Edinb. Dublin Philos. Mag. J. Sci.* **1923**, *46*, 836–871. [CrossRef]